Journal of Physics D: Applied Physics

PAPER

Is an extended barrier-free discharge under nanosecond-pulse excitation really diffuse?

To cite this article: Chenhua Ren *et al* 2022 *J. Phys. D: Appl. Phys.* **55** 235204

IOP Publishing Journal of Physics D: Applied Physics
J. Phys. D: Appl. Phys. **55** (2022) 235204 (10pp) https://doi.org/10.1088/1361-6463/ac4f0d

Is an extended barrier-free discharge under nanosecond-pulse excitation really diffuse?

Chenhua Ren[1,2], Bangdou Huang[2,*], Jintao Qiu[2,3], Cheng Zhang[2,3,*], Bo Qi[1], Weijiang Chen[4] and Tao Shao[2,3]

[1] North China Electric Power University, Beijing 102206, People's Republic of China
[2] Beijing International S&T Cooperation Base for Plasma Science and Energy Conversion, Institute of Electrical Engineering, Chinese Academy of Sciences, Beijing 100190, People's Republic of China
[3] University of Chinese Academy of Sciences, Beijing 100049, People's Republic of China
[4] State Grid Corporation of China, Beijing 100031, People's Republic of China

E-mail: huangbangdou@mail.iee.ac.cn and zhangcheng@mail.iee.ac.cn

Received 19 October 2021, revised 19 January 2022
Accepted for publication 26 January 2022
Published 11 March 2022

Abstract

A homogeneous discharge with a large volume is a desirable plasma source for many applications. Nanosecond-pulsed high-voltage (HV) excitation is believed to be a promising strategy for obtaining homogeneous or diffuse discharges at atmospheric pressure. In this paper, using a knife–plate geometry driven by a nanosecond-pulsed generator, a diffuse plasma sheet with a gap distance of 1 cm and a length of 12 cm is generated in atmospheric air, maintaining a low gas temperature of $\sim$330 K. However, time-resolved images reveal that the discharge, which appears diffuse to the naked eye, actually consists of multiple individual streamers that propagate from knife (HV) to plate (ground). The appearance of two processes, namely primary and secondary streamers, is consistently verified by discharge images, electric field evolution and fluid simulation. This further proves that the entire discharge belongs to an intermediate state between corona and spark. This work aids a deeper understanding of the intrinsic characters of similar diffuse discharges and optimizing parameters in practical applications.

Keywords: nanosecond pulsed discharge, diffuse plasma sheet, electric field-induced second-harmonic, plasma modeling, fluid model

(Some figures may appear in color only in the online journal)

1. Introduction

Atmospheric pressure non-thermal plasmas have received much attention due to their potential for use in many applications [1, 2], such as hydrogen production [3], surface modification [4, 5], biomedical sterilization [6, 7] and flow control [8, 9]. To improve application efficiency and control precision, homogeneous discharges with a large volume are more desirable [10, 11]. Typically, the high collision frequency in the atmosphere easily induces thermal-ionization instability and leads to a glow-to-arc transition [12, 13], which makes the generation of a homogeneous discharge challenging [14, 15].

With the development of nanosecond pulsed power technology, many efforts have been devoted to the formation of stable homogeneous discharges. With a sufficiently high pre-ionization level, electron avalanches can overlap before streamer formation [16–18]. Studies of volume discharges can be traced back to the middle of the last century [19–22]. By using x-rays as the pre-ionization source, a spatially homogeneous self-sustained discharge with a volume of several liters has been successfully generated at atmospheric pressure [22]. Even though the introduction of a dielectric barrier can stop streamer development and restrain the thermalization of the

* Authors to whom any correspondence should be addressed.

plasma channel, the limited gap distance restricts its available processing volume and is unfavorable for large-scale applications [14, 23]. With a repetition frequency of 40 kHz, the largest homogeneous discharge gap is extended up to 7 mm with dense seed electrons due to memory effects and a reduced gas density at a high temperature of 1300 K [10], which may be unsuitable for heat-sensitive applications such as biomedical engineering [24].

Unlike the plasma sources mentioned above, and without additional pre-ionization sources, a barrier-free diffuse discharge characterized by a large volume can be generated in an extremely inhomogeneous electric field [25–31]. As reported in [25, 26, 30], the gap bridged by diffuse discharges can reach several centimeters and no filaments or constricted channels are observed. A diffuse discharge can be generated under a flexible electrode geometry [25, 26, 32] and maintained over a wide range of operating parameters, such as pressure, gas type and mixture ratio, showing great potential for practical applications [33–35]. When applied with a high over-voltage and sub-nanosecond voltage fronts, a single large-volume streamer with a radius of several millimeters can be produced [25, 26, 30, 36]. Under these conditions runaway electrons may be generated and have an impact on discharge dynamics by providing a relatively high pre-ionization level [26, 30, 36]. However, if the high over-voltage level is decreased and the voltage rise time increased to several hundred nanoseconds, the diffuse form of the discharge can be maintained under an extremely inhomogeneous electric field, i.e. the knife–plate electrode configuration [37], but the temporal evolution of discharge during the ignition, propagation and connection of the electrode gap may be very different from the volume discharge. The reason for this is still not fully understood.

In this work, a transverse diffuse discharge is generated with a 1 cm air gap. Electrometry characteristics and dynamics of plasma propagation under a knife–plate geometry are investigated by experiments and numerical simulations.

2. Experimental methods and model description

Figure 1(a) shows the experimental electrode configuration and discharge image with an exposure time of 1 ms. The electrode system consists of a stainless-steel knife with length of 10 cm and thickness of 400 μm, and a copper plate with a length of 12 cm and width of 2.5 cm, between which a gap of 1 cm is kept. The knife is connected to a high-voltage (HV) unipolar positive nanosecond-pulse generator (Xi'an Lingfeng Electric Technology Co., Ltd) while the plate is grounded. The minimum rise time of the output voltage is $\sim$50 ns and the maximum amplitude is $\sim$23 kV. The repetition frequency of the voltage pulse is fixed at 50 Hz. Experiments were carried out in ambient air at atmospheric pressure at a temperature of around 25 °C and humidity of around 30%. As shown in the integral discharge image, a transverse uniform plasma sheet under the knife tip can be directly observed by the naked eye. The emitted luminosity is very intense near the HV electrode, and no filaments or constricted channels are formed.

The voltage waveform on the knife electrode is monitored by a HV probe (Tektronix, P6015A) and the current waveform is measured by a current probe (Pearson, 6595), both of which are recorded simultaneously by a digital oscilloscope (Lecroy WR204Xi). An intensified charge-coupled device (ICCD; Andor iStar sCMOS) camera is used to capture the discharge dynamics in the visible domain. Optical emission spectroscopy of the discharge is done with a spectrometer (PG-2000-Pro). Moreover, the electric field-induced second-harmonic (E-FISH) generation system is used to measure the temporal evolution of the electric field at different points within the gap [38, 39]. The 1064 nm fundamental output of a nanosecond Nd:YAG laser (Beamtech SGR-S400, pulse width 7–9 ns, and pulse energy $\sim$15 mJ) is focused on the discharge region, which remains parallel to the knife tip. The radius of a laser beam at the focus, measured by traversing a knife edge across the laser beam, is approximately 130 μm [38]. When using a lens with a shorter focal length, the beam radius around the focus will be less and the spatial resolution of the E-FISH measurement will be improved [40]. The intensities of the fundamental laser and the second-harmonic signal are detected by a photodiode (Thorlabs, DET10A2) and a photomultiplier (Hamamatsu, R1828-01), respectively. The calibration of the E-FISH signal is based on a parallel-plate electrode system (34 mm $\times$ 12 mm, gap 2.5 mm).

In this work, simulation is conducted with the two-dimensional (2D) PASSKEy (Parallel Streamer Solver with KinEtics) code [41], which has been used in modeling nanosecond-pulsed discharges [42–44]. Continuity equations with the drift-diffusion approximation, the energy conservation equation for mean electron energy, Poisson's equation for electric field and Helmholtz equations for photoionization are taken into account. Detailed descriptions of numerical approaches and mathematical formulations can be found in [43, 44]. As shown in figure 1(b), a 2D computational domain of size 3 cm $\times$ 2 cm is set up based on Cartesian (xy) coordinates, in which a 1 cm gap is adopted to approximate the side of a three-dimensional (3D) knife–plate configuration. The knife with a thickness w = 400 μm and tip radius r_{tip} = 15 μm is driven by a positive voltage pulse smoothed from the measured voltage, while the plate is grounded. A uniform mesh size of 8 μm is applied for the plasma domain and refined to 2 μm near the knife tip. Beyond the plasma domain, the mesh size grows exponentially. The plasma kinetics scheme for N_2/O_2 includes 15 species and 34 reactions. Detailed reactions and corresponding rates can be found in [43].

The numerical simulation mainly focuses on the case containing a series of pulses, not the very first pulse. The initial electron density before the next pulse can be enhanced. During the interval between two consecutive nanosecond pulses, the electron density n_{e} decays due to dissociative recombination [45, 46]

$$n_{\mathrm{e}}(t) \approx \frac{n_{\mathrm{e,max}}}{1 + k_{\mathrm{r}} n_{\mathrm{e,max}} t}.$$

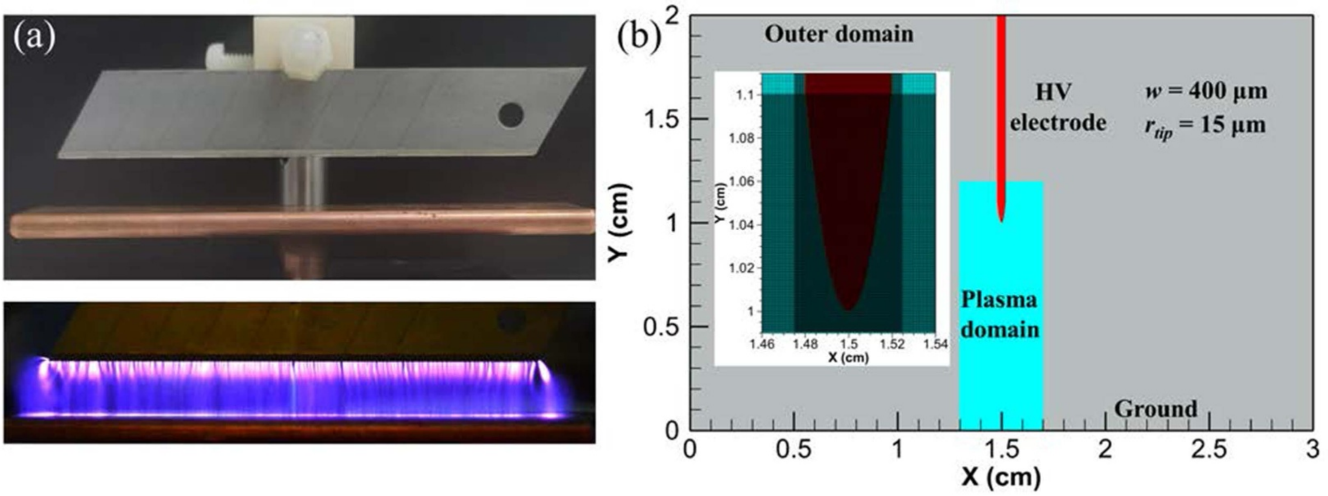

Figure 1. Geometric configuration of the knife–plate electrode and discharge image with an exposure time of 1 ms (a). Schematic of the computational domain in Cartesian coordinates (b).

Since O_4^+ is the main positive ion in the discharge channel during the late afterglow for atmospheric air [47], $k_r = 1.4 \times 10^{-12}(300/T_e)^{0.5}$ is taken as the dissociative recombination of electrons with O_4^+ ions [45, 46]. The maximum electron density $n_{e,max}$ is around 10^{20} m^{-3} (details are shown in the appendix) and t is 20 ms with pulse repetition of 50 Hz. When T_e changes from 1 to 0.1 eV, k_r changes from 2.25×10^{-13} m^3 s^{-1} to 7.12×10^{-13} m^3 s^{-1}, thus n_{e0} changes from 2.22×10^{14} m^{-3} to 7.02×10^{13} m^{-3} before the next pulse. As for the initial electron density, when the change exceeds more than an order of magnitude it may have a significant impact on the discharge properties. Thus, in the model, $n_{e0} = 10^{14}$ m^{-3} distributes uniformly in the plasma domain and the initial ion density is given based on quasi-neutrality.

3. Results and discussion

Figure 2(a) presents the waveforms of voltage and current obtained by measurement and simulation, respectively. The voltage pulse (V_{exp}) with a rise time of 50 ns, full width at half maximum (FWHM) of 130 ns and an amplitude of 15 kV is used to generate the diffuse plasma sheet. As for the measured total current waveform I_{exp}, two wider current peaks with different polarities appear in the rising and falling edges of V_{exp}, while one small peak with 6.4 A appears in the plateau. The displacement current obtained from $C \times dV/dt$ contributes to the majority of I_{exp} except for the plateau phase of V_{exp}, where C is the capacitance of the electrode system and dV/dt is the time derivative of V_{exp}. The conductive current I_c can be estimated by the difference between I_{exp} and $C \times dV/dt$, which reaches its maximum value at ~90 ns. Before the breakdown occurs, the measured current and the displacement current are theoretically identical. However, since the conductive current I_c is estimated from the difference between the two close values of I_{exp} and $C \times dV/dt$, the errors introduced by the differentiation process cause the fluctuations of I_c to be amplified. The signal delay on the cable also makes it difficult for I_{exp} and $C \times dV/dt$ to be completely consistent. Besides, due to the existence of stray capacitance and inductance in the circuit, some fluctuations are generated for I_{exp}. Thus, the obtained conductive current I_c presents some fluctuations before breakdown occurs and during the decline of the voltage pulse.

As for simulation, the waveform of V_{sim} smoothed from V_{exp} is adopted as the input voltage. The calculated current I_{sim} is the integral of fluxes of negative and positive charges through the surface of the HV electrode, consisting of a small spike of 1.1 A at 57 ns and a large peak of 7.3 A at 87 ns. The latter qualitatively agrees with I_c in both amplitude and temporal phase. The fact that the two current peaks have the same polarity indicates the presence of primary and secondary streamers in the discharge gap, different from the usual second current peak at the voltage falling phase which is due to a reversed electric field [48]. Similar phenomena can be found in other works [49, 50].

As shown in figure 2(b), the optical emission spectrum ranging from 280 to 430 nm is collected from the diffuse plasma sheet. It is clear that for the nanosecond-pulsed knife–plate discharge, the emission spectrum is dominated by the second positive system of molecular nitrogen $N_2(C^3\Pi_u–B^3\Pi_g)$. By fitting the measured spectrum of $N_2(C^3\Pi_u–B^3\Pi_g)$ with the Specair program [51], the rotational (T_{rot} = 330 K) and vibrational (T_{vib} = 3310 K) temperatures of N_2 are obtained. Since T_{vib} is much higher than T_{rot}, the extremely non-equilibrium plasma sheet enhances chemical activity [10], occupying unique advantages in diverse applications such as processing of heat-sensitive materials and sterilization of biological tissue.

Figure 3 shows the evolution of single-shot images for the knife–plate discharge taken by an ICCD camera during the voltage pulse. The gate width of the ICCD is 3 ns and the delay time between the two consecutive images is 2 ns. The image of

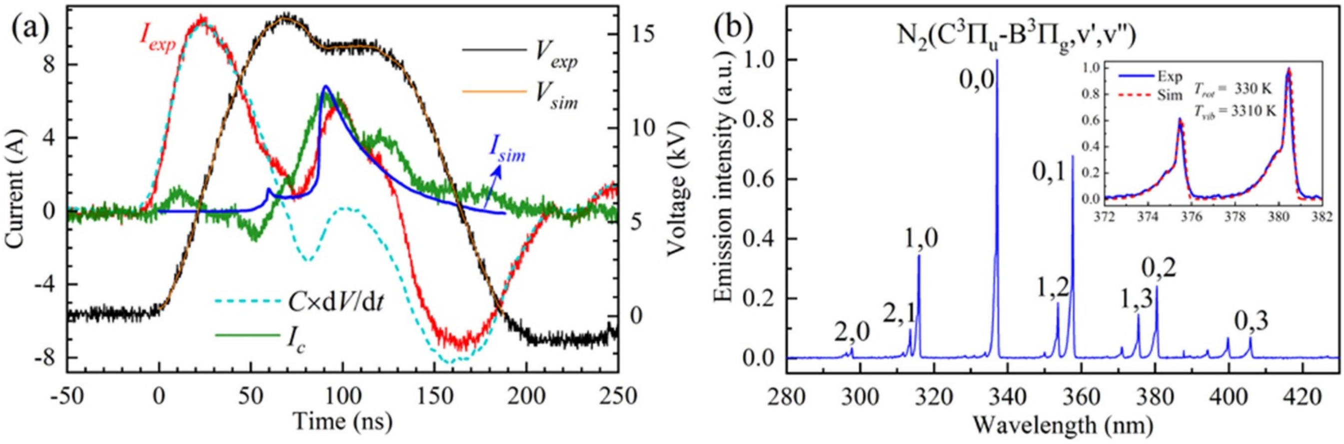

Figure 2. Waveforms of voltage and current from both measurement and simulation (a) and optical emission spectrum of the discharge (b).

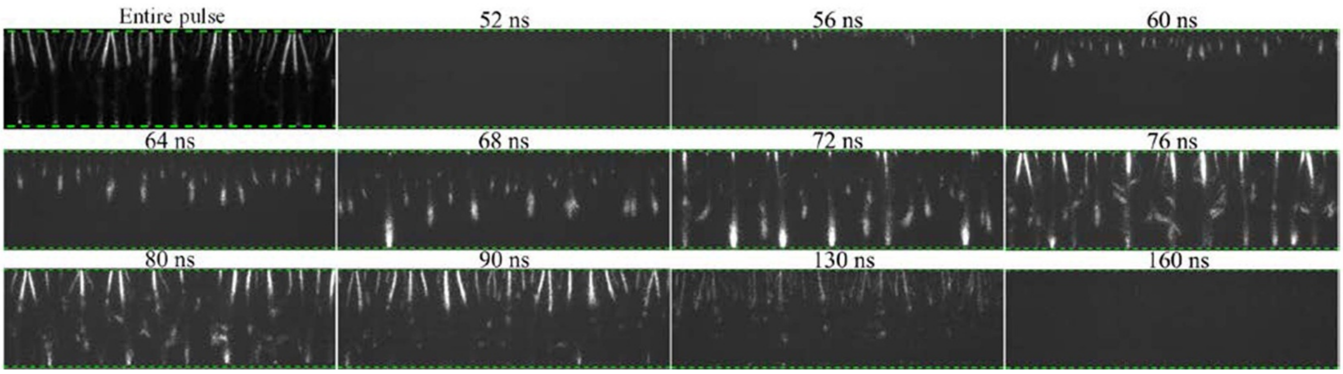

Figure 3. Temporal evolution of the knife–plate discharge (camera gate 3 ns) with a peak voltage of 15 kV taken by an ICCD camera (single-shot). The entire pulse image is also shown (camera gate 150 ns).

one discharge pulse with a gate of 150 ns is also presented. The two dashed lines indicate the location of the knife and plate electrodes, respectively. As shown in the single-shot image, the plasma sheet, which appears uniform to the naked eye, actually consists of multiple individual streamers, whose light emission is more intense near the knife tip but becomes rather weak below it. At 52 ns, a weak luminous spot is generated at the knife tip and no plasma can be found before that, indicating discharge breakdown (primary streamer). Afterwards, several discharge spots gradually appear at different locations along the knife tip and propagate towards the plate (52–72 ns). A dark region is left behind the primary streamer fronts. At 68 ns, one streamer reaches the plate first and then more streamers arrive step by step (72 ns). The mean propagation velocity of the primary streamers can be roughly estimated as $(5.0–6.3) \times 10^5$ m s^{-1}.

After reaching the ground, primary streamers quickly extinguish while multiple luminous channels, i.e. secondary streamers, appear again in the vicinity of the knife tip, which looks much brighter than the former. When a pre-ionized channel is present the electric field E is much lower than that of the primary streamer [50, 52, 53]. Thus, secondary streamers only propagate about 3–4 mm away from the HV electrode, i.e. the secondary streamers do not punch through the discharge gap. During the period with secondary streamers, luminescence exists along the entire discharge gap due to the left-over channel of primary streamers. The entire discharge is more intensified than a corona, but is inhibited from transition to a spark [26]. The development of secondary streamers is very rapid, but can be maintained for a relatively long time (72–90 ns). Subsequently, secondary streamers fade away until they are completely extinguished at 160 ns as the voltage continues to decrease.

The calculated temporal evolutions of n_e, $N_2(C^3\Pi_u)$ density and E are shown in figure 4. The maximum electron density occurs at the HV electrode first, then decreases slightly during the propagation of the primary streamer and rises again as the plate is approached. After the discharge front has passed by, the reduction of T_e in the channel makes n_e decrease due to rapid recombination processes, for example $e + O_4^+ \rightarrow 2O + O_2$ with a rate of $1.4 \times 10^{-12}(300/T_e)^{0.5}$ [45, 46], especially near the HV electrode. The drop in n_e weakens the shielding effect caused by space charge in the channel, and the high potential applied on the HV electrode is maintained; both these effects make E near the knife tip exceed the breakdown threshold again and trigger the secondary streamer [45].

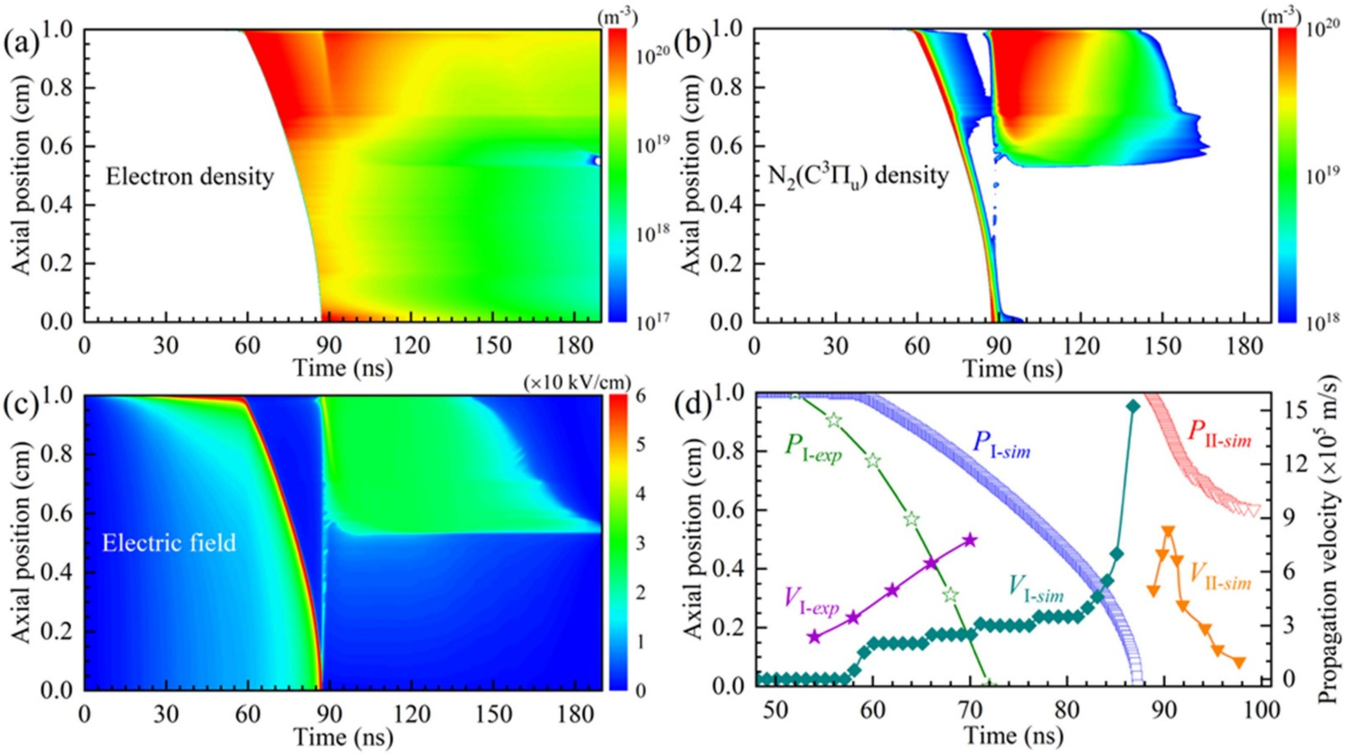

Figure 4. Temporal evolution of calculated n_e (a), $N_2(C^3\Pi_u)$ (b) and E (c) along the streamer propagation axis $x = 1.5$ cm, and dynamics (location and velocity) of the ionization front obtained by measurement and simulation (d).

Moreover, since the discharge emission intensity is proportional to molecular density on the upper energy level of the spectral band, the distribution of $N_2(C^3\Pi_u)$ can be used to characterize the discharge kinetics [42]. During the primary streamer propagation, the maximum $N_2(C^3\Pi_u)$ density is mainly concentrated on the discharge front and rapidly diminishes after the front passes. In contrast, as for the secondary streamer, $N_2(C^3\Pi_u)$ density keeps a continuous profile along the discharge channel and decays slowly versus time. The calculated discharge dynamics and morphology are consistent with the ICCD images.

The maximum E appears at the front of the primary streamer, while during the secondary streamer phase E is uniformly distributed along the discharge channel near the knife tip and drops remarkably in the remaining gap. Between the primary and secondary streamers, a return stroke propagates towards the anode at an extremely fast velocity. A similar phenomenon is also obtained in both experiments and simulations [31, 36, 50, 52, 53].

Figure 4(d) presents the locations of the measured and calculated discharge fronts (P, hollow symbols) and corresponding instantaneous speeds (V, solid symbols) for the primary (I) and secondary streamers (II), respectively. The position of the maximum $N_2(C^3\Pi_u)$ at $x = 1.5$ cm is selected to represent the location of the discharge front. It is clear that the calculated primary streamer ignites at ∼56 ns and reaches the ground at ∼87 ns, taking about 31 ns to penetrate the discharge gap. Its speed continues to increase during the propagation and shows a significant increment as it approaches the ground. As for the secondary streamer, the farthest reachable distance from the HV electrode (∼4 mm) is obtained at 98 ns and its propagation velocity first increases and then drops remarkably within ∼8 ns. Thus, the small spike in I_{sim} indicates the initiation of the primary streamer, and the large peak is contributed by both the breakdown of the primary streamer and the initiation of the secondary streamer.

For comparison, the discharge dynamics of the fastest batch of primary streamers obtained from ICCD images are also shown. Obviously, in the experiment, it takes less time to cross the discharge gap. Note that, the knife–plate discharge is essentially a 3D phenomenon and the radius of curvature of the steamer head should be smaller than in 2D simulation [54]. Besides, the selection of r_{tip} for the knife in the simulation greatly affects the discharge properties. A smaller r_{tip} enhances the discharge intensity. The roughness of the knife electrode causes streamers to ignite at different locations in the experiments. Nevertheless, as more primary streamers arrive at the ground, the discharge current pulse I_c reaches its maximum gradually at around 90 ns, showing excellent agreement with I_{sim}, as shown in figure 1(a).

Figure 5(a) presents the temporal evolution of the measured electric field at different locations by the E-FISH method. As the voltage begins to increase, E first increases near the HV electrode (1.0 cm), while it remains unchanged close to the ground (0.0 cm), which also means that it is a Laplacian field before the breakdown happens. After E at the knife tip reaches

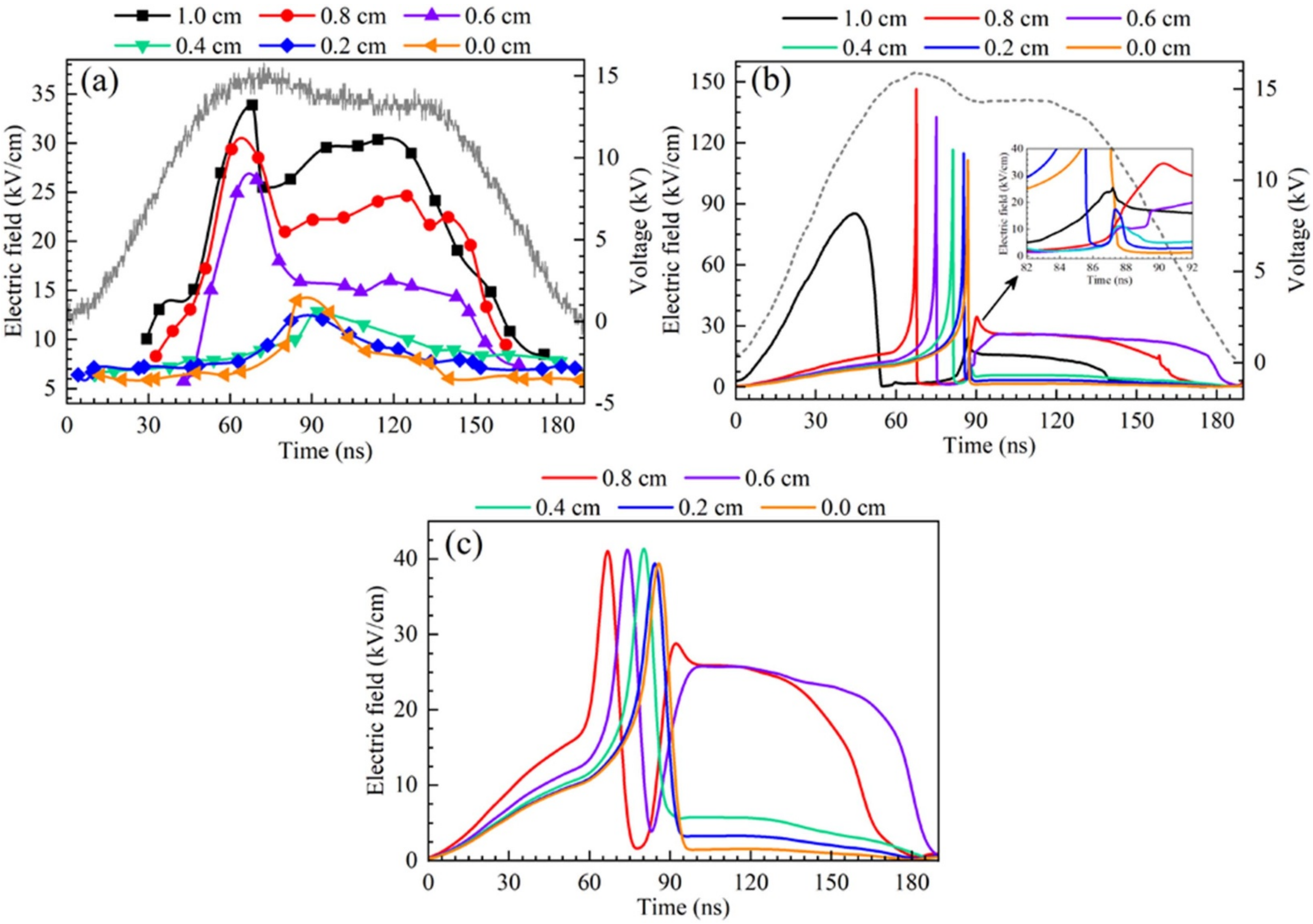

Figure 5. Temporal evolution of measured (a) and calculated (b) E at different locations in the knife–plate discharge gap. Convolution of calculated E with a Gaussian laser pulse (c).

a peak of 34 kV cm^{-1}, it starts to drop and then a decrease in the amplitude of E also occurs at locations further away from the HV electrode, indicating the process of propagation of the primary streamer. Subsequently, only E near the knife tip increases again and reaches its second peak, which corresponds to the secondary streamer. When the applied voltage decreases, E in the discharge gap diminishes to a low level.

Similarly, in the simulation, a two-peak feature is observed for the electric field near the knife and in the middle of discharge gap, but only one peak is obtained near the plate (figure 5(b)). The second peak of the calculated E near the knife tip corresponds to the secondary streamer, while near the plate it is induced by a reverse ionization wave as the primary streamer approaches the plate.

However, the most distinct difference between the measurement and simulation is that the peak value of the electric field in the simulation is more than four times higher than the measured one. This is due to the extremely fast propagation speed and the limitation of temporal resolution of the E-FISH system (7–9 ns) [38]. As shown in figure 5(c), after convolution between the calculated E and a Gaussian laser pulse (FWHM $\sim$ 8 ns), an average electric field can be obtained, which is closer to the measured E. Thus, although the nanosecond E-FISH system can measure the variation of E in a shorter time than the laser pulse [55], the peak is greatly underestimated, especially during streamer development. For further investigation, a femtosecond or picosecond laser is more desirable [40, 56].

4. Summary and conclusions

In summary, characteristics of the knife–plate discharge operated in atmospheric pressure air were studied experimentally and numerically. Excited by a nanosecond-pulsed generator, a diffuse plasma sheet was formed with a gap of 1 cm. Discharge dynamics obtained by the ICCD camera demonstrate that the plasma sheet, which appears diffuse to the naked eye, actually consists of multiple individual streamers, including primary and secondary streamers. The primary streamers can penetrate the discharge gap and quickly extinguish after reaching the plate, while the secondary streamers only propagate about 3–4 mm away from the HV electrode. Although the diffuse discharge generated in the knife–plate electrode geometry is not completely homogeneous, the short voltage pulse restricts the thermal-ionization instability and maintains the entire discharge in an intermediate state between corona and spark. Both current and discharge dynamics in the experiment qualitatively agree with the calculated results. Even though a 2D electrode geometry was used to generate diffuse discharge and 2D simulation can capture the dominant features of discharge propagation dynamics, the 3D structure of individual streamer is still an important factor for further investigation.

Data availability statement

All data that support the findings of this study are included within the article (and any supplementary files).

Acknowledgments

This work was supported by the National Science Fund for Distinguished Young Scholars (Grant No. 51925703), the National Natural Science Foundation of China (Grant Nos. 52022096 and 51907190), and the Royal Society–Newton Advanced Fellowship, UK (Grant No. NAF/R2/192117).

Appendix

To illustrate the influence of the initial electron density n_{e0} on the discharge properties, the calculated results with three different n_{e0} values ranging from 10^{12} to 10^{14} m^{-3} are shown below. As for the calculated current (figure 6), the increment in n_{e0} makes the breakdown occur earlier and elevates the amplitude of the second peak, while it reduces the first peak slightly. The temporal evolution of electron density, $N_2(C^3\Pi_u)$ density and electric field at two different locations (0.2 and 0.8 cm away from the HV electrode) is also presented (figure 7). For these three cases, the temporal evolution of electron density and $N_2(C^3\Pi_u)$ density shows a two-peak feature near the HV electrode, but only one peak near the ground, all of which indicate that the discharge consists of a primary and secondary streamer phase. Although n_{e0} varies by two orders of magnitude, the calculated results show that the maximum electron density, $N_2(C^3\Pi_u)$ density and electric field change slightly. For example, when n_{e0} varies from 10^{12} to 10^{14} m^{-3}, $n_{e,max}$ changes from 4.4×10^{20} to 4.7×10^{20} at a location of 0.2 cm away from the HV electrode. Thus, the value of n_{e0} has a little effect on $n_{e,max}$.

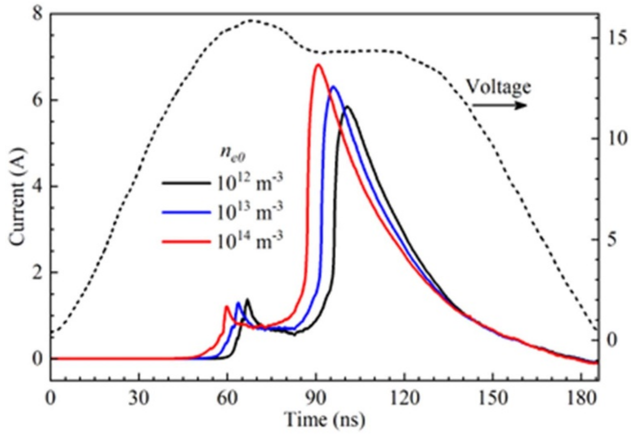

Figure 6. Calculated current with different initial electron density n_{e0}.

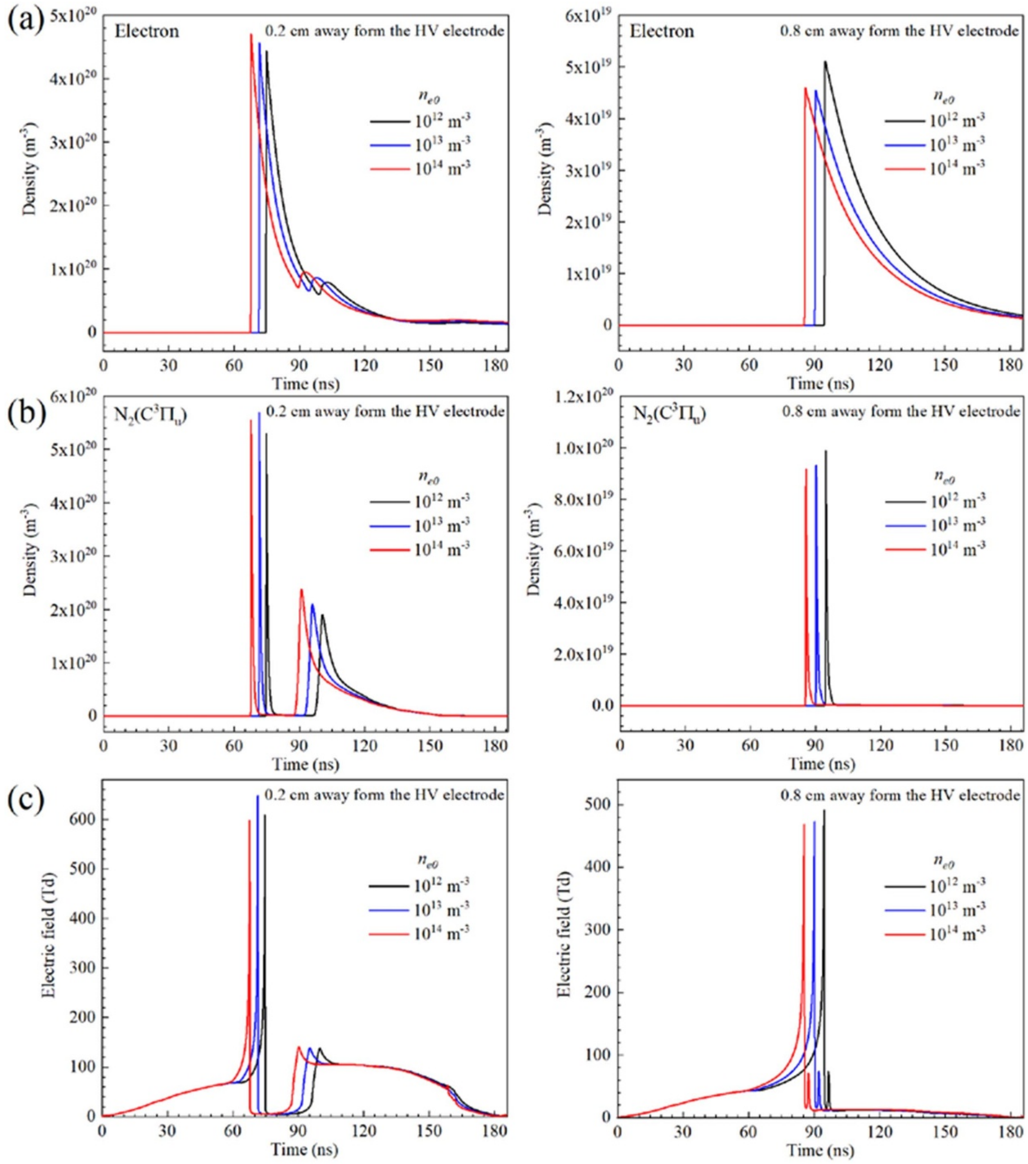

Figure 7. Temporal evolutions of (a) electron density, (b) $N_2(C^3\Pi_u)$ density and (c) electric field with different n_{e0} at locations 0.2 cm (left) and 0.8 cm (right) away from the HV electrode.

ORCID iDs

Chenhua Ren https://orcid.org/0000-0002-7163-1171
Bangdou Huang https://orcid.org/0000-0002-1523-7380
Cheng Zhang https://orcid.org/0000-0003-1512-2820
Bo Qi https://orcid.org/0000-0001-8001-5824
Tao Shao https://orcid.org/0000-0002-5738-1241

References

[1] Park S, Choe W, Lee H, Park J Y, Kim J, Moon S Y and Cvelbar U 2021 Stabilization of liquid instabilities with ionized gas jets *Nature* **592** 49
[2] Jia P, Gao K, Zhou S, Chen J, Wu J, Wu K and Li X 2021 Morphology evolution of an atmospheric pressure glow discharge initiated in the air gap between a liquid cathode and a needle anode *Plasma Sources Sci. Technol.* **30** 095021
[3] Xu S *et al* 2019 Sustaining metal–organic frameworks for water-gas shift catalysis by non-thermal plasma *Nat. Catal.* **2** 142
[4] Dou S, Tao L, Wang R, El Hankari S, Chen R and Wang S 2018 Plasma-assisted synthesis and surface modification of electrode materials for renewable energy *Adv. Mater.* **30** 1705850
[5] Turicek J, Ratts N, Kaltchev M and Masoud N 2021 Investigation of a helium tubular cold atmospheric pressure plasma source and polymer surface treatment application *Plasma Sources Sci. Technol.* **30** 025005
[6] Kim J, Kim J H, Chang B, Choi E H and Park H 2016 Hemorheological alterations of red blood cells induced by non-thermal dielectric barrier discharge plasma *Appl. Phys. Lett.* **109** 193701
[7] Athanasopoulos D, Svarnas P, Ladas S, Kennou S and Koutsoukos P 2018 On the wetting properties of human stratum corneum epidermidis surface exposed to cold atmospheric-pressure pulsed plasma *Appl. Phys. Lett.* **112** 213703
[8] Xu H, He Y, Strobel K L, Gilmore C K, Kelley S P, Hennick C C, Sebastian T, Woolston M R, Perreault D J and Barrett S R H 2018 Flight of an aeroplane with solid-state propulsion *Nature* **563** 532
[9] Gomez-Vega N, Xu H, Abel J M and Barrett S R H 2021 Performance of decoupled electroaerodynamic thrusters *Appl. Phys. Lett.* **118** 074101
[10] Qi F, Li Y, Zhou R, Wang J, Xian Y, Cullen P J, Lu X and Ostrikov K 2019 Uniform atmospheric pressure plasmas in a 7 mm air gap *Appl. Phys. Lett.* **115** 194101
[11] Ren C, He X, Jia P, Wu K and Li X 2020 Influence of asymmetric degree on the characteristics of a homogeneous barrier discharge excited by an asymmetric sine *Phys. Plasmas* **27** 113507
[12] Li L, Liu L, Liu Y, Bin Y, Ge Y and Lin F 2014 Analysis and experimental study on formation conditions of large-scale barrier-free diffuse atmospheric pressure air plasmas in repetitive pulse mode *J. Appl. Phys.* **115** 023301
[13] Stepanyan S A, Starikovskiy A Y, Popov N A and Starikovskaia S M 2014 A nanosecond surface dielectric barrier discharge in air at high pressures and different polarities of applied pulses: transition to filamentary mode *Plasma Sources Sci. Technol.* **23** 045003
[14] Chen S, Heijmans L C J, Zeng R, Nijdam S and Ebert U 2015 Nanosecond repetitively pulsed discharges in N_2–O_2 mixtures: inception cloud and streamer emergence *J. Phys. D: Appl. Phys.* **48** 175201
[15] Wang Y, Yan H, Guo H, Xu Y, Zhang Q and Song J 2021 Evolution of the uniformity in the repetitive unipolar nanosecond-pulse dielectric barrier discharge *Plasma Sources Sci. Technol.* **30** 075009
[16] Raizer Y P 1991 *Gas Discharge Physics* (Berlin: Springer)
[17] Palmer A J 1974 A physical model on the initiation of atmospheric-pressure glow discharges *Appl. Phys. Lett.* **25** 138
[18] Osipov V V 2000 Self-sustained volume discharge *Phys.-Usp.* **43** 221
[19] Basov N G, Belenov E M, Danilychev V A and Suchkov A F 1971 High-pressure pulsed CO_2 laser *Sov. J. Quantum Electron.* **1** 306
[20] Fenstermacher C A, Nutter M J, Leland W T and Boyer K 1972 Electron-beam-controlled electrical discharge as a method of pumping large volumes of CO_2 laser media at high pressure *Appl. Phys. Lett.* **20** 56
[21] Mesyats G A and Korolev Y D 1986 High-pressure volume discharges in gas lasers *Sov. Phys.-Usp.* **29** 57
[22] Lin S and Levatter J I 1979 X-ray preionization for electric discharge lasers *Appl. Phys. Lett.* **34** 505
[23] Shao T, Long K, Zhang C, Yan P, Zhang S and Pan R 2008 Experimental study on repetitive unipolar nanosecond-pulse dielectric barrier discharge in air at atmospheric pressure *J. Phys. D: Appl. Phys.* **41** 215203
[24] Lv Y, Nie L, Duan J, Li Z and Lu X 2021 Cold atmospheric plasma jet array for transdermal drug delivery *Plasma Process. Polym.* **18** e2000180
[25] Tardiveau P, Moreau N, Bentableb S, Postel C and Pasquiers S 2009 Diffuse mode and diffuse-to-filamentary transition in a high pressure nanosecond scale corona discharge under high voltage *J. Phys. D: Appl. Phys.* **42** 175202
[26] Shao T, Zhang C, Zheng N, Yan P, Tarasenko V F, Baksht E K, Burahenko A G and Shutko Y V 2011 Diffuse discharge, runaway electron, and x-ray in atmospheric pressure air in an inhomogeneous electrical field in repetitive pulsed modes *Appl. Phys. Lett.* **98** 021503
[27] Starikovskiy A Y 2011 Fast ionization wave development in atmospheric-pressure air *IEEE Trans. Plasma Sci.* **39** 2602
[28] Tardiveau P, Magne L, Marode E, Ouaras K, Jeanney P and Bournonville B 2016 Sub-nanosecond time resolved light emission study for diffuse discharges in air under steep high voltage pulses *Plasma Sources Sci. Technol.* **25** 054005
[29] Babaeva N Y, Zhang C, Qiu J, Hou X, Tarasenko V F and Shao T 2017 The role of fast electrons in diffuse discharge formation: Monte Carlo simulation *Plasma Sources Sci. Technol.* **26** 085008
[30] Tarasenko V F, Panchenko A N and Beloplotov D V 2020 Diffuse and volume discharges in high-pressure gas lasers pumped by transverse discharge (a review) *Plasma Phys. Rep.* **46** 850
[31] Bourdon A, Pechereau F, Tholin F and Bonaventura Z 2021 Study of the electric field in a diffuse nanosecond positive ionization wave generated in a pin-to-plane geometry in atmospheric pressure air *J. Appl. Phys.* **54** 075204
[32] Zhang C, Shao T, Yan P and Zhou Y 2014 Nanosecond-pulse gliding discharges between point-to-point electrodes in open air *Plasma Sources Sci. Technol.* **23** 035004
[33] Shao T, Wang R, Zhang C and Yan P 2018 Atmospheric-pressure pulsed discharges and plasmas: mechanism, characteristics and applications *High Voltage* **3** 14
[34] Zhang C, Qiu J, Kong F, Hou X, Fang Z, Yin Y and Shan T 2018 Plasma surface treatment of Cu by nanosecond-pulse diffuse discharges in atmospheric air *Plasma Sci. Technol.* **20** 014011
[35] Naidis G V, Tarasenko V F, Babaeva N Y and Lomaev M I 2018 Subnanosecond breakdown in high-pressure gases *Plasma Sources Sci. Technol.* **27** 013001

[36] Beloplotov D V, Tarasenko V F, Shklyaev V A and Sorokin D A 2021 Generation of runaway electrons in plasma after a breakdown of a gap with a sharply non-uniform electric field strength distribution *J. Appl. Phys.* **54** 304001

[37] Shao T, Zhang C, Zhou Y, Xie Q, Zhou Z and Yan P 2014 Diffuse discharges in open air sustained by microsecond and nanosecond pulses *IEEE Trans. Plasma Sci.* **42** 2408

[38] Huang B, Zhang C, Adamovich I V, Akishev Y and Shao T 2020 Surface ionization wave propagation in the nanosecond pulsed surface dielectric barrier discharge: the influence of dielectric material and pulse repetition rate *Plasma Sources Sci. Technol.* **29** 044001

[39] Huang B, Zhang C, Zhu W, Lu X and Shao T 2021 Ionization waves in nanosecond pulsed atmospheric pressure plasma jets in argon *High Voltage* **6** 665

[40] Dogariu A, Goldberg B M, O'Byrne S and Miles R B 2017 Species-independent femtosecond localized electric field measurement *Phys. Rev. Appl.* **7** 024024

[41] Zhu Y, Chen X, Wu Y and Starikovskaia S 2021 PASSKEy code [software] (Paris: Science and Technology of Plasma Dynamics Laboratory, Xi'an, China and Laboratoire de Physique des Plasmas) (available at: www.plasma-tech.net/parser/passkey/)

[42] Zhu Y, Shcherbanev S, Baron B and Starikovskaia S 2017 Nanosecond surface dielectric barrier discharge in atmospheric pressure air: i. measurements and 2D modeling of morphology, propagation and hydrodynamic perturbations *Plasma Sources Sci. Technol.* **26** 125004

[43] Zhu Y and Starikovskaia S 2018 Fast gas heating of nanosecond pulsed surface dielectric barrier discharge: spatial distribution and fractional contribution from kinetics *Plasma Sources Sci. Technol.* **27** 124007

[44] Zhu Y, Chen X, Wu Y, Hao J, Ma X, Lu P and Tardiveau P 2021 Simulation of ionization-wave discharges: a direct comparison between the fluid model and E-FISH measurements *Plasma Sources Sci. Technol.* **30** 075025

[45] Zhu Y and Wu Y 2020 The secondary ionization wave and characteristic map of surface discharge plasma in a wide time scale *New J. Phys.* **22** 103060

[46] Soloviev V R, Anokhin E M and Aleksandrov N L 2020 Spatial distribution of radiation emitted by pulsed surface dielectric barrier discharge in air *Plasma Sources Sci. Technol.* **29** 035006

[47] Pancheshnyi S V and Starikovskii A Y 2004 Stagnation dynamics of a cathode-directed streamer discharge in air *Plasma Sources Sci. Technol.* **13** B1

[48] Pan J, Tan Z, Wang X, Sha C, Nie L and Chen X 2014 Effects of pulse parameters on the atmospheric pressure dielectric barrier discharges driven by the high-voltage pulses in Ar and N_2 *Plasma Sources Sci. Technol.* **23** 065019

[49] Zhang C, Huang B, Luo Z, Che X, Yan P and Shao T 2019 Atmospheric-pressure pulsed plasma actuators for flow control: shock wave and vortex characteristics *Plasma Sources Sci. Technol.* **28** 064001

[50] Ono R and Komuro A 2020 Generation of the single-filament pulsed positive streamer discharge in atmospheric-pressure air and its comparison with two-dimensional simulation *J. Phys. D: Appl. Phys.* **53** 035202

[51] Laux C O, Spence T G, Kruger C H and Zare R N 2003 Optical diagnostics of atmospheric pressure air plasmas *Plasma Sources Sci. Technol.* **12** 125

[52] Ono R and Oda T 2003 Formation and structure of primary and secondary streamers in positive pulsed corona discharge-effect of oxygen concentration and applied voltage *J. Phys. D: Appl. Phys.* **36** 1952

[53] Ono R 2016 Optical diagnostics of reactive species in atmospheric-pressure nonthermal plasma *J. Phys. D: Appl. Phys.* **49** 083001

[54] Cruccolini V, Scarcelli R, Battistoni M, Grimaldi C N, Dal R M A, Breden D and Raja L L 2020 Multidimensional modeling of non-equilibrium plasma generated by a radio-frequency corona discharge *Plasma Sources Sci. Technol.* **29** 115013

[55] Adamovich I V, Butterworth T, Orriere T, Pai D Z, Lacoste D A and Cha M S 2020 Nanosecond second harmonic generation for electric field measurements with temporal resolution shorter than laser pulse duration *J. Phys. D: Appl. Phys.* **53** 145201

[56] Orr K, Yang X, Gulko I and Adamovich I V 2020 Formation and propagation of ionization waves during ns pulse breakdown in plane-to-plane geometry *Plasma Sources Sci. Technol.* **29** 125022